

**Efficient calculation of self-energy matrices for electron-transport simulations**Yoshiyuki Egami,<sup>1,\*</sup> Shigeru Tsukamoto,<sup>2</sup> and Tomoya Ono<sup>3</sup><sup>1</sup>*Division of Applied Physics, Faculty of Engineering, Hokkaido University, Sapporo, Hokkaido 060-8628, Japan*<sup>2</sup>*Peter Grünberg Institut & Institute for Advanced Simulation, Forschungszentrum Jülich and JARA, D-52425 Jülich, Germany*<sup>3</sup>*Department of Electrical and Electronic Engineering, Kobe University, Kobe, Hyogo 657-8501, Japan*

(Received 26 April 2019; revised manuscript received 21 July 2019; published 7 August 2019)

The computational cost of calculating the self-energy matrices used in first-principles transport-property calculations is proportional to the cube of the lateral length of electrodes. Therefore, the clarification of transport properties is difficult because the system size increases when the transition region structure becomes complicated owing to lattice defects such as adatoms, substitutional doping, vacancies, and lattice distortions. In this study we propose an improved procedure to calculate the self-energy matrices in the electrodes to reduce computational costs of electron-transport calculations without degrading the accuracy. This procedure accurately reproduces the self-energy matrices of the supercell-structured electrodes from the generalized Bloch states of the primitive unit cell. Furthermore, we carry out electron-transport calculations on fluorine-adsorbed graphene sheets connected to semi-infinite graphene electrodes and find the dependence of the electron transmission on the symmetry of the arrangement of adatoms perpendicular to the transport direction.

DOI: [10.1103/PhysRevB.100.075413](https://doi.org/10.1103/PhysRevB.100.075413)**I. INTRODUCTION**

In the last decade, two-dimensional materials attracted a lot of interest, and their electron-transport properties have been investigated not only for exploring fundamental physics but also for applying them to novel electronic devices. Among the various two-dimensional materials, graphene is recognized as an essential material; hence it has been frequently used as a platform for electron-transport measurement and simulation, where the graphene platform is modified to tune the electron-transport properties by adsorbing a heteroatom/molecule [1–5], introducing point/line defects [6–9], substituting the C atoms with heteroatoms [10–14], and so on. It is clearly seen that increasing the complexity of the chemically/physically modified graphene platforms, the system size to be dealt with also increases. Therefore, the computational cost for calculating the electron-transport properties of such two-dimensional systems increases drastically as the complexity increases. This growth in computational cost obviously prevents us from investigating the electron-transport properties of realistic systems, and forces us to introduce some approximations and accuracy deterioration.

Aiming at reducing the computational cost of electron-transport calculations without deteriorating accuracy, we have so far studied how to improve the electron-transport calculation method based on the wave function matching formula. One of the bottlenecks in calculating the electron-transport properties of a two-dimensional system with a pair of semi-infinite electrodes is the computational cost for calculating the self-energy matrices of the semi-infinite electrodes. More specifically, the length of the electrode unit cells in the direction perpendicular to the electron flow is restricted to be

the same as that of the adjoining transition region. Therefore, the computational cost of the self-energy matrices increases proportionally to the cubic of the transversal length of the transition region. Even if a small primitive unit cell is just tiled and filled in the electrode unit cell in the transversal direction, one has to calculate the self-energy matrices of the large electrode unit cell. So far, many researchers have struggled to calculate self-energy matrices with low computational cost [15–17], and have achieved a reduction in computational costs by using some approximations. In this paper we tackle the problem of improving the highly inefficient calculation of self-energy matrices without introducing any approximation and deteriorating accuracy.

As an application of the improved electron-transport calculation method, we study the electron-transport properties of graphene sheets modified by fluorine adsorption. More specifically, we investigate the possibility of tuning electron transmission by changing the density and adsorption site of fluorine atoms. The transmission in the vicinity of the Fermi level can be greatly reduced even if the adatom density is small. By contrast, the several conduction channels with transmission peaks according to the density of the adatoms were observed in the high incident energy region. Furthermore, in the direction perpendicular to the transport direction, the difference between the structural symmetry of the fluorine atoms adsorbed on the graphene surface and the spatial symmetry of the incident Bloch waves inside the electrodes affects the peak value of the electron transmission. In addition, we describe the procedure for improving the computational accuracy of the calculation for the transmission and reflection coefficients in the Appendix.

The rest of this paper is composed as follows: Section II presents the theoretical procedure used to construct the self-energy matrices of an extended unit cell with a large transversal dimension based on the generalized Bloch states

\*Corresponding author: [y\\_egami@eng.hokudai.ac.jp](mailto:y_egami@eng.hokudai.ac.jp)

of the corresponding primitive unit cell. Section III demonstrates our method of examining the transport properties of fluorinated graphene models and reveals how the transport property is influenced by the concentration and arrangement of the adatom. Section IV provides the conclusions. Appendix A describes the method for accurately calculating the transmission/reflection coefficient from scattering wave functions. Appendices B and C describe some of the mathematical techniques used in this paper.

## II. SELF-ENERGY MATRIX OF A SUPERCELL-STRUCTURED ELECTRODE

In general, an electrode unit cell employed in transport calculations has a simpler geometry than a transition region, and can be divided into smaller primitive unit cells. All the physical quantities of the electrode, such as the self-energy matrix, can be in principle obtained from the calculations for the small primitive unit cell, i.e., one need not treat a large electrode unit cell that is composed by just repeating a primitive unit cell. In this section we propose an efficient procedure for calculating the self-energy matrix of a semi-infinite electrode in a supercell structure, in which a primitive unit cell is repeated in the directions parallel to the electrode surface like as a crystal. This section is composed of three subsections: First, we briefly present the conventional way to calculate the self-energy matrix of a semi-infinite electrode. Second, we derive a procedure for the self-energy matrix of a supercell-structured electrode based on the conventional way, and show that it is not practical. Third, we discuss a more promising and less expensive procedure.

### A. Conventional procedure

Here we briefly describe a conventional procedure to derive the self-energy matrix of a leftward semi-infinite electrode from a set of the generalized Bloch states of the corresponding bulk system [18,19]. In an electrode part far away from the surface, the effective potential can be considered to converge to that of the corresponding bulk system, and therefore, to be periodic. The Hamiltonian matrix  $\mathbf{H}$  of the electrode unit cell repeats along the unit-cell index  $\dots, \ell-1, \ell, \ell+1, \dots$  as shown in Fig. 1, and is independent of  $\ell$ . The interaction between the adjoining unit cells represented by matrix  $\mathbf{B}$  is also independent of the unit-cell index  $\ell$ . On the basis of the real-space finite-difference formalism [20] within the framework of the density functional theory [21], the dimension of  $\mathbf{B}$  is finite, and we can regard  $\mathbf{B}$  as a  $N_{\mathbf{B}}$ -dimensional square matrix. In general,  $N_{\mathbf{B}}$  is smaller than the dimension of  $\mathbf{H}$ . Accordingly, the  $i$ th generalized Bloch state of a periodic bulk system with respect to energy  $\varepsilon$  satisfies the following Kohn-Sham equation:

$$\begin{bmatrix} \mathbf{0} & \mathbf{0} & \mathbf{B}^\dagger \\ \vdots & \ddots & \mathbf{0} \\ \mathbf{0} & \dots & \mathbf{0} \end{bmatrix} \begin{bmatrix} \mathbf{q}_{i,\ell-1,1} \\ \vdots \\ \mathbf{q}_{i,\ell-1,N} \end{bmatrix} + (\varepsilon - \mathbf{H}) \begin{bmatrix} \mathbf{q}_{i,\ell,1} \\ \vdots \\ \mathbf{q}_{i,\ell,N} \end{bmatrix} \\ + \begin{bmatrix} \mathbf{0} & \dots & \mathbf{0} \\ \mathbf{0} & \ddots & \vdots \\ \mathbf{B} & \mathbf{0} & \mathbf{0} \end{bmatrix} \begin{bmatrix} \mathbf{q}_{i,\ell+1,1} \\ \vdots \\ \mathbf{q}_{i,\ell+1,N} \end{bmatrix} = \mathbf{0}. \quad (1)$$

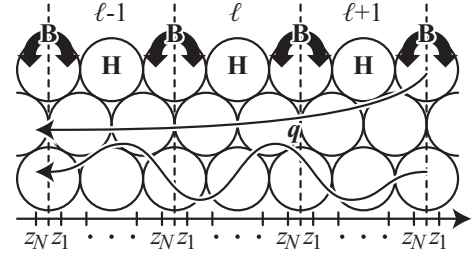


FIG. 1. Schematic representation of an electrode part away from the surface. Unit cells are indexed as  $\dots, \ell-1, \ell, \ell+1, \dots$ , and the real-space grids in each unit cell are indexed as  $z_1, \dots, z_N$ .  $\mathbf{H}$  and  $\mathbf{B}$  represent the Hamiltonian of a unit cell and the interaction between the adjoining unit cells. Note that the dimension of  $\mathbf{B}$  is finite within the framework of the real-space finite-difference formalism. The curves with arrows represent the leftward propagating/decaying generalized Bloch waves, which are referred to as  $\mathbf{q}$  in the text.

Here  $\mathbf{q}_{i,\ell-1,1(N)}$ ,  $\mathbf{q}_{i,\ell,1(N)}$ , and  $\mathbf{q}_{i,\ell+1,1(N)}$  represent the wave function vector at  $z = z_{1(N)}$  in the  $(\ell-1)$ th,  $\ell$ th, and  $(\ell+1)$ th unit cells, respectively. The length of the subvectors is  $N_{\mathbf{B}}$ , i.e.,  $N_{\mathbf{B}}$  is generally the number of real-space grids on an  $xy$  plane at  $z = z_i$  or can be an integer multiple of it. Note that the superscript  $\dagger$  denotes the conjugate transpose of a matrix. The Kohn-Sham equation is known to have  $2N_{\mathbf{B}}$  independent solutions, as far as  $\mathbf{B}$  is a regular matrix [22]. Half of the solutions represents the leftward propagating/decaying generalized Bloch wave functions, and the rest is the rightward propagating/decaying ones, as depicted in Fig. 1.

Collecting the  $N_{\mathbf{B}}$  leftward propagating/decaying generalized Bloch waves in the  $\ell$ th unit cell,  $\mathbf{q}_{i,\ell,N}$  for  $i = 1, \dots, N_{\mathbf{B}}$ , we define matrix

$$\mathbf{Q}_{\mathbf{L}} = [\mathbf{q}_{1,\ell,N}, \dots, \mathbf{q}_{N_{\mathbf{B}},\ell,N}]. \quad (2)$$

In the same way, we define another matrix composed of the  $N_{\mathbf{B}}$  leftward propagating/decaying generalized Bloch waves in the  $(\ell+1)$ th unit cell, i.e.,  $\mathbf{q}_{i,\ell+1,N}$  for  $i = 1, \dots, N_{\mathbf{B}}$ :

$$\mathbf{Q}_{\mathbf{R}} = [\mathbf{q}_{1,\ell+1,1}, \dots, \mathbf{q}_{N_{\mathbf{B}},\ell+1,1}]. \quad (3)$$

It is clearly seen that  $\mathbf{Q}_{\mathbf{L}}$  and  $\mathbf{Q}_{\mathbf{R}}$  are both  $N_{\mathbf{B}}$ -dimensional regular matrices and are invertible [23]. Consequently, we define the following matrix:

$$\mathbf{R}_{\mathbf{L}} = \mathbf{Q}_{\mathbf{L}} \mathbf{Q}_{\mathbf{R}}^{-1}, \quad (4)$$

which represents the ratio of the generalized Bloch wave functions at  $z = z_N$  in the  $\ell$ th unit cell to those at  $z = z_1$  in the  $(\ell+1)$ th unit cell. Note that  $\mathbf{R}_{\mathbf{L}}$  is independent of  $\ell$ . When  $\mathbf{R}_{\mathbf{L}}$  operates on any subvector at  $z = z_1$  in a unit cell, the vector is transferred into a subvector at  $z = z_N$  in the left adjoining unit cell. The self-energy matrix of a leftward semi-infinite electrode  $\Sigma_{\mathbf{L}}$  is known to be obtained as the matrix product of the interaction matrix  $\mathbf{B}$  and the ratio matrix  $\mathbf{R}_{\mathbf{L}}$  [24]:

$$\Sigma_{\mathbf{L}} = \mathbf{B}^\dagger \mathbf{R}_{\mathbf{L}}. \quad (5)$$

It is obvious that the self-energy matrix of a rightward semi-infinite electrode  $\Sigma_{\mathbf{R}}$  can be straightforwardly derived by collecting the  $N_{\mathbf{B}}$  rightward propagating/decaying generalized Bloch waves.

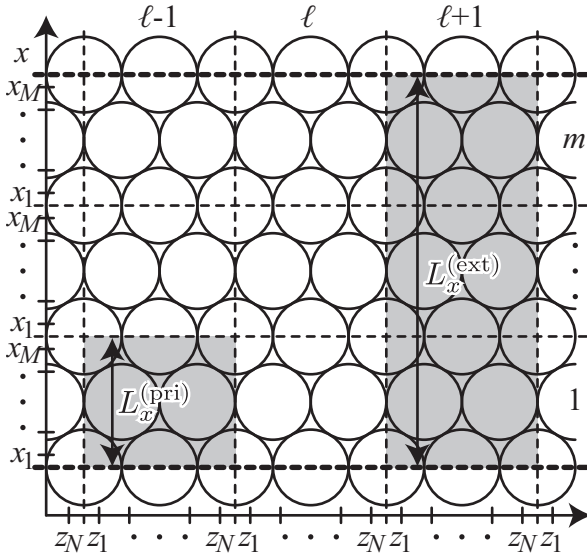


FIG. 2. Schematic representation of a primitive unit cell and a supercell. The small gray area indicates a primitive unit cell, whereas the large one shows a supercell. The supercell is composed of  $m$  primitive unit cells repeated along the  $x$  direction.  $M$  denotes the number of real-space grids in a primitive unit cell in the  $x$  direction.  $L_x^{(\text{pri})}$  and  $L_x^{(\text{ext})}$  represent the unit-cell and supercell lengths in the  $x$  direction, respectively.

### B. Extending generalized Bloch wave functions

Let us now discuss the case of a semi-infinite electrode in a supercell structure in the directions parallel to the electrode surface. For simplicity we consider the case in which a primitive unit cell is repeated for  $m$  times only in the  $x$  direction to form a supercell structure, as depicted in Fig. 2. Although we do not explicitly take into account any  $k$  points in the  $x$  direction in Sec. II A, hereafter we explicitly treat discrete  $k$  points in the  $x$  direction with respect to a primitive unit cell defined as

$$k_{x,j}^{(\text{pri})} = k_{x,0}^{(\text{pri})} + \frac{2\pi}{L_x^{(\text{pri})}} \frac{j-1}{m}, \quad (6)$$

for  $j = 1, \dots, m$ , where  $L_x^{(\text{pri})}$  represents the length of the primitive unit cell in the  $x$  direction.  $k_{x,0}^{(\text{pri})}$  denotes an offset of the set of the  $k$  points and is given as

$$0 \leq k_{x,0}^{(\text{pri})} < \frac{2\pi}{L_x^{(\text{pri})}}. \quad (7)$$

Since generalized Bloch states are obtained by solving Eq. (1) for each  $k_{x,j}^{(\text{pri})}$ , the matrices composed of  $N_{\mathbf{B}}$  generalized Bloch wave functions are also defined for each  $j$  as

$$\mathbf{Q}_L^{(j)} = [\mathbf{q}_{1,\ell,N}^{(j)}, \dots, \mathbf{q}_{N_{\mathbf{B}},\ell,N}^{(j)}], \quad (8)$$

$$\mathbf{Q}_R^{(j)} = [\mathbf{q}_{1,\ell+1,1}^{(j)}, \dots, \mathbf{q}_{N_{\mathbf{B}},\ell+1,1}^{(j)}]. \quad (9)$$

A column vector  $\mathbf{q}_{i,\ell,k}^{(j)}$  represents the portion of the  $i$ th generalized Bloch wave function at  $z = z_k$  in the  $\ell$ th primitive unit cell obtained for the  $j$ th  $k$ -point  $k_{x,j}^{(\text{pri})}$ . According to the Bloch's theorem, a generalized Bloch wave function over a supercell is obtained by multiplying that of the corresponding

primitive unit cell by the Bloch's phase factors

$$a_{I,J} = \frac{1}{\sqrt{m}} \exp [ik_{x,j}^{(\text{pri})}(I-1)L_x^{(\text{pri})}], \quad (10)$$

for  $I = 1, \dots, m$ , where  $1/\sqrt{m}$  is a normalization factor. Consequently, the set of leftward propagating and decaying generalized Bloch wave function vectors of the supercell at  $k_x^{(\text{ext})} = k_{x,0}^{(\text{pri})}$  is expressed as

$$\tilde{\mathbf{Q}}_X = \begin{bmatrix} a_{1,1}\mathbf{Q}_X^{(1)} & \cdots & a_{1,m}\mathbf{Q}_X^{(m)} \\ \vdots & \ddots & \vdots \\ a_{m,1}\mathbf{Q}_X^{(1)} & \cdots & a_{m,m}\mathbf{Q}_X^{(m)} \end{bmatrix}, \quad (11)$$

where  $X$  stands for L or R. The matrix  $\tilde{\mathbf{Q}}_{L(R)}$  is obviously  $m$  times as large as  $\mathbf{Q}_{L(R)}^{(j)}$  in both the row and column dimensions, i.e.,  $mN_{\mathbf{B}}$ , and is also invertible. In analogy with the discussion in Sec. II A, we can determine the self-energy matrix of the leftward semi-infinite supercell-structured electrode  $\tilde{\Sigma}_L$  as

$$\tilde{\Sigma}_L = \tilde{\mathbf{B}}^\dagger \tilde{\mathbf{R}}_L \quad \text{where} \quad \tilde{\mathbf{R}}_L = \tilde{\mathbf{Q}}_L \tilde{\mathbf{Q}}_R^{-1}. \quad (12)$$

Here  $\tilde{\mathbf{R}}_L$  denotes the ratio matrix of the supercell, and  $\tilde{\mathbf{B}}$  represents the interaction between the adjoining supercells in the  $z$  direction. It is, however, difficult to calculate the inverse of  $\tilde{\mathbf{Q}}_R$  in a practical computation, because the dimension of the matrix is generally too large and the computational cost is  $O[(mN_{\mathbf{B}})^3]$ . Therefore, computing  $\tilde{\Sigma}_L$  according to the aforementioned recipe is very time consuming and impractical. Since solving Eq. (1) for all the generalized Bloch states deteriorates the accuracy, one may use the recursive procedure, which calculates  $\tilde{\mathbf{R}}_L$  only from propagating and slowly decaying generalized Bloch states, to avoid accuracy deterioration [9,18,19]. Nevertheless this procedure requires us to calculate the inverse of  $\tilde{\mathbf{R}}_L$ , which also costs  $O[(mN_{\mathbf{B}})^3]$ . Therefore, we conclude that extending the generalized Bloch wave functions is straightforward to calculate  $\tilde{\Sigma}_L$  but is inefficient and impractical.

### C. Extending singular vectors

In this subsection we propose an efficient procedure to calculate the self-energy matrix of a supercell-structured electrode. First, it is assumed that we have already obtained the ratio matrices for the corresponding primitive unit cell  $\mathbf{R}_L^{(j)}$  for  $j = 1, \dots, m$ . By using the singular-value decomposition [25],  $\mathbf{R}_L^{(j)}$  is expressed as the product of three matrices:

$$\mathbf{R}_L^{(j)} = \mathbf{U}_L^{(j)} \mathbf{S}_L^{(j)} [\mathbf{V}_L^{(j)}]^\dagger, \quad (13)$$

where  $\mathbf{S}_L^{(j)}$  is the diagonal matrix composed of the singular values of  $\mathbf{R}_L^{(j)}$ , and  $\mathbf{U}_L^{(j)}$  and  $\mathbf{V}_L^{(j)}$  are the left and right singular matrices composed of the left and right singular vectors, respectively. Note that the three matrices are all  $N_{\mathbf{B}}$ -dimensional square matrices. One can see that the singular vectors are periodic in the  $x$  direction, because  $\mathbf{R}_L^{(j)}$  is essentially composed of the generalized Bloch wave functions of the primitive unit cell that are periodic in the  $x$  direction, as seen from Eq. (4).

In analogy with the discussion in Sec. II B, one can extend each singular vector of the primitive unit cell over the supercell by multiplying the vector by the Bloch's phase factors

$a_{l,j}$  for  $l = 1, \dots, m$ . Consequently, the left and right singular vector matrices of the supercell are expressed as

$$\tilde{\mathbf{U}}_L = \begin{bmatrix} a_{1,1}\mathbf{U}_L^{(1)} & \cdots & a_{1,m}\mathbf{U}_L^{(m)} \\ \vdots & \ddots & \vdots \\ a_{m,1}\mathbf{U}_L^{(1)} & \cdots & a_{m,m}\mathbf{U}_L^{(m)} \end{bmatrix} \quad (14)$$

and

$$\tilde{\mathbf{V}}_L = \begin{bmatrix} a_{1,1}\mathbf{V}_L^{(1)} & \cdots & a_{1,m}\mathbf{V}_L^{(m)} \\ \vdots & \ddots & \vdots \\ a_{m,1}\mathbf{V}_L^{(1)} & \cdots & a_{m,m}\mathbf{V}_L^{(m)} \end{bmatrix}, \quad (15)$$

respectively. The singular-value matrix of the supercell is composed of  $\mathbf{S}^{(j)}$  for  $j = 1, \dots, m$  and is expressed as the following block-diagonal matrix:

$$\tilde{\mathbf{S}}_L = \begin{bmatrix} \mathbf{S}_L^{(1)} & \mathbf{0} & \mathbf{0} \\ \mathbf{0} & \ddots & \mathbf{0} \\ \mathbf{0} & \mathbf{0} & \mathbf{S}_L^{(m)} \end{bmatrix}. \quad (16)$$

Therefore, the ratio matrix of the supercell is given as the product of three  $mN_B$ -dimensional square matrices:

$$\tilde{\mathbf{R}}_L = \tilde{\mathbf{U}}_L \tilde{\mathbf{S}}_L [\tilde{\mathbf{V}}_L]^\dagger. \quad (17)$$

The self-energy matrix of the leftward semi-infinite supercell-structured electrode is, finally, given as

$$\tilde{\Sigma}_L = \tilde{\mathbf{B}}^\dagger \tilde{\mathbf{R}}_L. \quad (18)$$

It should be noted that this procedure to calculate  $\tilde{\Sigma}_L$  does not include inverting any large matrices, and thus, it is obviously less costly in practical computation.

It is already known that  $\mathbf{R}_L^{(j)}$  can be accurately calculated only from propagating and slowly decaying generalized Bloch states by using a recursive procedure [9,18,19]. Therefore, we do not need to perform an expensive computation to calculate all generalized Bloch states. In the recursive procedure, one has to calculate numerically the inverse of a matrix with the same dimension to  $\mathbf{R}_L^{(j)}$ . The computational cost for inverting all  $\mathbf{R}_L^{(j)}$  for  $j = 1, \dots, m$  is only  $O[mN_B^3]$ , while that for inverting  $\tilde{\mathbf{R}}_L$  is  $O[(mN_B)^3]$ . The present method is, therefore, more efficient in calculating the self-energy matrix of a semi-infinite electrode in a supercell structure in the directions parallel to the electrode surface. It should be noticed that the aforementioned procedure for extending the ratio matrix using singular-value decomposition is also applicable for extending Green's function in the directions perpendicular to the electrode surface because the basis functions composing Green's function are also periodic in these directions.

#### D. Accuracy test

In this section we verify that the procedure proposed in Sec. II C does not deteriorate the accuracy. For this verification we employ a Si(001)-1  $\times$  1 bulk system with a tetragonal primitive unit cell that contains four Si atoms. The dimensions of the primitive unit cell are set to  $L_x^{(\text{pri})} = L_y^{(\text{pri})} = 3.84 \text{ \AA}$  ( $=7.26 a_B$ ), and  $L_z^{(\text{pri})} = 5.43 \text{ \AA}$  ( $=10.3 a_B$ ) [26]. The supercell employed here has a dimension in the  $x$  direction that is two times as long as that of the primitive unit cell,

i.e.,  $L_x^{(\text{ext})} = 2L_x^{(\text{pri})}$ . This corresponds to  $m = 2$  in Fig. 2. The other dimensions are the same as those of the primitive unit cell, i.e.,  $L_y^{(\text{ext})} = L_y^{(\text{pri})}$  and  $L_z^{(\text{ext})} = L_z^{(\text{pri})}$ . We evaluate the accuracy by comparing the self-energy matrix obtained by Eq. (5) for the extended unit cell and that obtained by Eq. (18). In this subsection the former is referred to as  $\Sigma_L^{\text{ref}}$  and the latter is referred to as  $\tilde{\Sigma}_L$ . To perform the accuracy verification without loss of generality for  $k$  points, we calculate  $\Sigma_L^{\text{ref}}$  and  $\tilde{\Sigma}_L$  for a nonzero  $k$  point in the  $x$  direction of the supercell, i.e.,  $k_x^{(\text{ext})} = 0.2 \times 2\pi/L_x^{(\text{ext})}$ , which corresponds to  $k_{x,0}^{(\text{pri})} = 0.1 \times 2\pi/L_x^{(\text{pri})}$ . Using the electronic structure calculation code RSPACE [18,27], which is an implementation of the real-space finite-difference formalism, the effective potential of the primitive unit cell is calculated with  $8 \times 8 \times 6$   $k$  points and the finite-difference order  $N_f = 4$  [20]. The effective potential of the supercell is obtained by repeating that of the primitive unit cell in the  $x$  direction. The calculations are carried out with the norm-conserving pseudopotentials proposed by Troullier and Martins [28,29] and with the local-density approximation [30] within the framework of the density functional theory [21].

Figures 3(a) and 3(b) show the absolute and relative errors in  $\tilde{\Sigma}_L$  with respect to  $\Sigma_L^{\text{ref}}$  evaluated for each entry of the matrices as

$$[\text{absolute error}]_{ij} = |[\tilde{\Sigma}_L]_{ij} - [\Sigma_L^{\text{ref}}]_{ij}| \quad (19)$$

and

$$[\text{relative error}]_{ij} = \frac{[\text{absolute error}]_{ij}}{|[\Sigma_L^{\text{ref}}]_{ij}|}, \quad (20)$$

respectively. Here  $[\mathbf{X}]_{ij}$  denotes the  $(i, j)$ th entry of a matrix  $\mathbf{X}$ . One can see in Fig. 3(a) that the absolute errors are not more than  $10^{-10}$  and the large errors appear mainly in the submatrix at around the upper-left corner, which operates on a wave function at the interface between a transition region and a lead. In Fig. 3(c) the full-width at half-maximum of the absolute errors is found to be from  $10^{-16}$  to  $10^{-12}$ , implying large distribution of the absolute errors. However, from Figs. 3(b) and 3(d) it turns out that the relative errors are approximately  $10^{-9}$  over the whole matrix and the dispersion is small. We conclude that  $\tilde{\Sigma}_L$  obtained for the supercell is accurately reproduced by the method proposed in Sec. II C.

We also verify that the proposed method is applicable to extending a Green's function matrix as well as a ratio matrix, as mentioned in the last of Sec. II C. For this verification, we extend the tetragonal Si(001) primitive unit cell into a  $2 \times 2$  supercell, i.e.,  $L_x^{(\text{ext})} = 2L_x^{(\text{pri})}$  and  $L_y^{(\text{ext})} = 2L_y^{(\text{pri})}$ , and adopt  $k_x^{(\text{ext})} = 0.2 \times 2\pi/L_x^{(\text{ext})}$  and  $k_y^{(\text{ext})} = 0.2 \times 2\pi/L_y^{(\text{ext})}$ , which correspond to  $k_{x,0}^{(\text{pri})} = 0.1 \times 2\pi/L_x^{(\text{pri})}$  and  $k_{y,0}^{(\text{pri})} = 0.1 \times 2\pi/L_y^{(\text{pri})}$ , respectively. The other calculation conditions are the same as those used for the verification of  $\tilde{\Sigma}_L$ . Computational error in the Green's function matrix obtained by the proposed method  $\tilde{\mathbf{G}}_L$  with respect to that obtained by inverting a truncated Hamiltonian matrix of an extended system  $\mathbf{G}_L^{(\text{ref})}$  is evaluated through Eqs. (19) and (20) with  $\tilde{\mathbf{G}}_L$  and  $\mathbf{G}_L^{(\text{ref})}$  instead of  $\tilde{\Sigma}_L$  and  $\Sigma_L^{\text{ref}}$ . Figures 3(e) and 3(f) show the histograms of the absolute and relative errors of  $\tilde{\mathbf{G}}_L$  with respect to  $\mathbf{G}_L^{(\text{ref})}$ . Both absolute and relative errors are

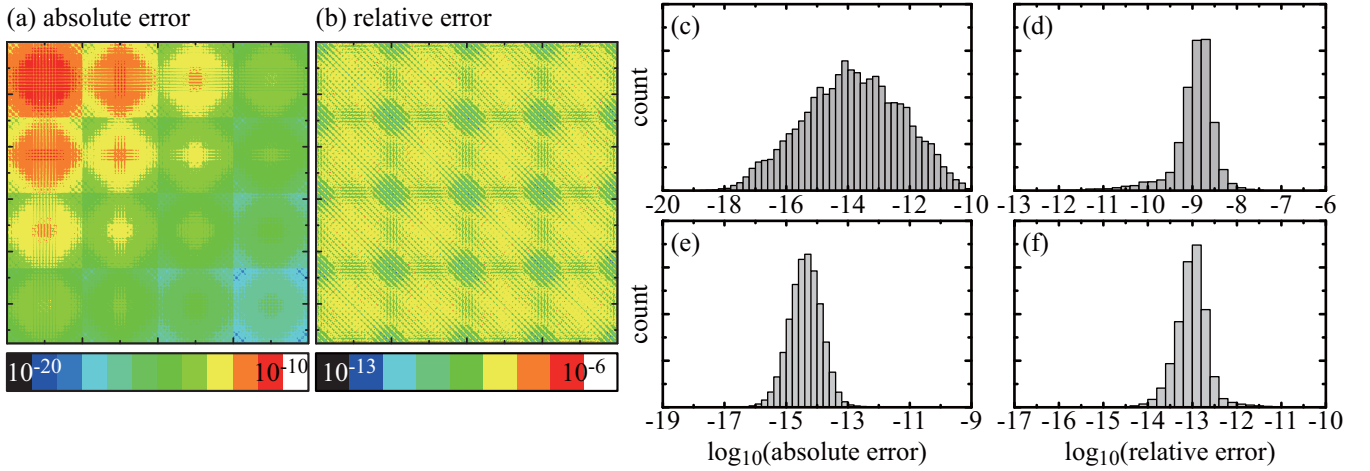


FIG. 3. Computational error brought by the proposed method. The computational error in  $\tilde{\Sigma}_L$  with respect to  $\Sigma_L^{\text{ref}}$  is shown in (a)–(d), and that in  $\tilde{G}_L$  with respect to  $G_L^{\text{ref}}$  in (e) and (f). The contour maps (a) and (b) represent the absolute and relative errors calculated by Eqs. (19) and (20), respectively. The histograms (c)–(f) are shown as a function of error in logarithmic scale.

small enough, and  $\tilde{G}_L$  is correctly reproduced by the proposed method. Consequently, we conclude that the proposed method is available to extend a Green’s function matrix in the  $x$  and/or  $y$  directions as well as a self-energy matrix.

Furthermore, we compare the computational time in generating the self-energy terms for several supercell models according to Eq. (5) with that in reproducing them using Eq. (18). The results are summarized in Table I. The computational time for a primitive cell is obtained by averaging the computational times for the primitive cell with various wave numbers  $k_{x(y),0}^{(\text{pri})}$ . For generating  $\Sigma_L$ , the computational time increases proportional to  $N^3$ , where  $N$  is the number of the total grid points in the supercell. In some cases, the computational efficiency exceeds the theoretical value (the square of the supercell size) because the order of the computational time for the recursive iteration

to generate the self-energy terms is slightly larger than  $N^3$ . On the other hand, the computational time for reproducing  $\tilde{\Sigma}_L$  is significantly reduced by the proposed method, and this benefit becomes more remarkable as the supercell size increases.

In addition, in order to investigate the efficiency of reduction of computational time by using our method, the ratio of the computational time required by generating the self-energy matrices to that for calculating the electron-transport properties is demonstrated. Here the electron-transport property of a model in which some Si atoms in the Si (001) bulk are replaced with N atoms is calculated. The scattering region consists of 459 Si atoms and 5 N atoms, and the dimensions of the cell are set to  $L_x^{(\text{ext})} = L_y^{(\text{ext})} = 15.4 \text{ \AA} (=29.0 a_B)$ , and  $L_z^{(\text{ext})} = 38.0 \text{ \AA} (=71.8 a_B)$ , and the number of grids is  $48 \times 48 \times 112$  with  $N_f = 4$ . In large-scale systems it is

TABLE I. Computational time to generate and to reproduce self-energy terms. The computational efficiency is evaluated as [generating time]/[reproducing time]. The calculations are performed on a single core of Intel®Xeon®CPU Gold 6130. The number of recursive iteration to generate each ratio matrix is 20 [9]. The finite-difference order  $N_f$  is 4.

Primitive model [number of grids]	Supercell size	Computational time (s)		Computational efficiency
		Generate $\Sigma_L$	Reproduce $\tilde{\Sigma}_L$	
Si(001)	$1 \times 1$	15.4	–	–
[ $12 \times 12 \times 16$ ]	$2 \times 1$	117.7	30.8	3.8
4 Si atoms	$2 \times 2$	1 058.4	68.4	15.5
	$4 \times 4$	82 168.1	435.7	188.6
Al(001)	$1 \times 1$	63.1	–	–
[ $16 \times 16 \times 16$ ]	$2 \times 1$	585.6	134.1	4.1
4 Al atoms	$2 \times 2$	5 119.7	278.9	18.4
	$4 \times 1$	5 253.9	284.7	18.5
Al(111)	$1 \times 1$	383.3	–	–
[ $16 \times 28 \times 40$ ]	$2 \times 1$	3 471.9	828.3	4.2
12 Al atoms	$2 \times 2$	32 610.0	1 701.6	19.2
Zigzag graphene	$1 \times 1$	8701.5	–	–
[ $20 \times 60 \times 16$ ]	$2 \times 1$	87 316.9	18 514.1	4.7
4 C atoms	$4 \times 1$	677 154.4	38 346.2	17.7

difficult to perform self-consistent transport property calculations because the computational cost is proportional to the cube of the system size. However, non-self-consistent calculations can also provide transport properties with an adequate accuracy. The electrode structure is obtained by arranging primitive cells containing 4 Si atoms, which are the same as mentioned above, in  $4 \times 4$  in the  $xy$  directions, and there are 16 Si atoms at the interface between the scattering and the electrode regions. The transport property calculation is collectively performed for 24 incident electron energy points, and a computational CPU time required per energy point (an energy point of 1.0 eV above the Fermi energy is sampled) is estimated. This calculation is performed on Intel®Xeon®CPU E5-2680. The computational CPU time for generating the self-energy matrices using Eq. (5) is 485 661 s (the ratio to the total CPU time is 27.0%). On the other hand, when the self-energy matrices are reproduced from the those of 16 primitive cells using Eq. (18), the computational CPU time can be reduced to 1113 s (the ratio to the total CPU time is 0.1%). The proposed method is more useful for larger systems as shown in Table I. Moreover, the transmission probabilities obtained based on the respective formulas coincide with the accuracy of the relative error of  $10^{-7}$ . Thus, it is confirmed that electron-transport properties can be estimated efficiently without deterioration of computational accuracy using our method.

In order to apply the advantages of the proposed method to practical calculations, we analyze and compare the electron-transport properties of chemically modified graphenes with different geometrical structures in the following section.

### III. APPLICATIONS

Recently, graphene-based electronic devices such as field-effect transistors have attracted significant attention because of the excellent electrical, mechanical, and optical properties of the graphene [1,31–33]. Graphene has a zero band gap at the  $K$  and  $K'$  points in the Brillouin zone, where the conduction and valence bands touch each other in the charge neutrality point. For electronic applications, it is important to open a finite energy gap and to tune the band structure.

The electronic structures of graphene can be drastically changed by a chemical modification, such as atomic adsorption on the surface, and can be tuned by the density and arrangement of adatoms. When a hydrogen or a fluorine atom is adsorbed on a carbon atom [5,34–39], electron conductivity is suppressed because the  $\pi$  orbitals extending over the pristine graphene surface are terminated. However, discussions on the influence of the difference in symmetry of the structure on the electron-transport properties are still ongoing. In this section we perform transport simulations of electrons flowing through the fluorinated graphene to examine the influence of the structural symmetry on the transport properties.

Figure 4 illustrates the computational models wherein a partially fluorinated graphene is connected to semi-infinite pristine graphene electrodes. The adatoms are adsorbed on both sides of the graphene, and the fluorinated carbon dimers are arranged along the transport direction ( $z$  direction) where the carbon atom making C-C bonds is converted from a

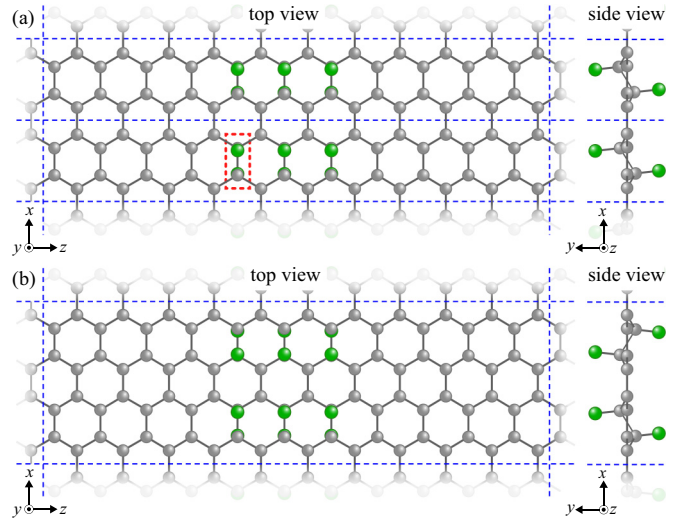


FIG. 4. Schematic views of the unit cells of the (a) CFG model and the (b) IFG model. The blue dashed lines indicate the cell boundaries. The gray and green spheres represent the C and F atoms, respectively. The models with  $N_d = 3$ , which is the number of fluorinated carbon dimers in the  $x$  direction, are illustrated (a fluorinated carbon dimer is surrounded by red dotted lines).

$sp^2$  (a flat plane) to  $sp^3$ -like (a buckled graphene) configuration [5,12,34,35,38] (the fluorinated carbon dimer is surrounded by red dotted lines in Fig. 4). In the current study we consider two types of symmetry of the arrangement of the fluorinated carbon dimers to examine the influence of the structural symmetry in the  $x$  direction perpendicular to the transport direction on the transport properties. One is the buckled configuration being commensurate with the neighbor dimers in the  $x$  direction [Fig. 4(a)]. In the other type of models, the buckled configuration is opposite to the neighbor in the  $x$  direction [Fig. 4(b)]. Here and hereafter we refer to the fluorinated graphene structures in Figs. 4(a) and 4(b) as the *commensurate* fluorinated graphene (CFG) model and the *incommensurate* fluorinated graphene (IFG) model, respectively. In the electron-transport calculations, since the electrodes for the IFG model are twice as wide as those for the CFG model, the self-energy matrices for the IFG model can be calculated from those for the CFG models without significant increase in computational cost by using the proposed method. We also explore the influence of the density of adatoms on the electron-transport properties, where the number of fluorinated carbon dimers in the  $z$  direction  $N_d$  varies between two and four.

We first optimize the atomic and electronic structures of the models. First-principles calculations using the RSPACE code [18,27] were performed. For the optimization calculations of atomic structures, periodic boundary conditions are imposed in all directions. In the CFG (IFG) model, the side lengths of the unit cell in the lateral direction parallel to the graphene surface are taken as  $4.26(8.52) \times 27.1 \text{ \AA}^2$  and a repeating sheet model is separated by  $12.7 \text{ \AA}$  in the  $y$  direction perpendicular to the graphene surface. The number of grid points in the real space is  $24(48) \times 72 \times 176$ , the finite-difference order  $N_f = 4$ , and there are 44 (88) C and  $2(4) \times N_d$  F atoms in the unit cell of the CFG (IFG) model. The Brillouin zone

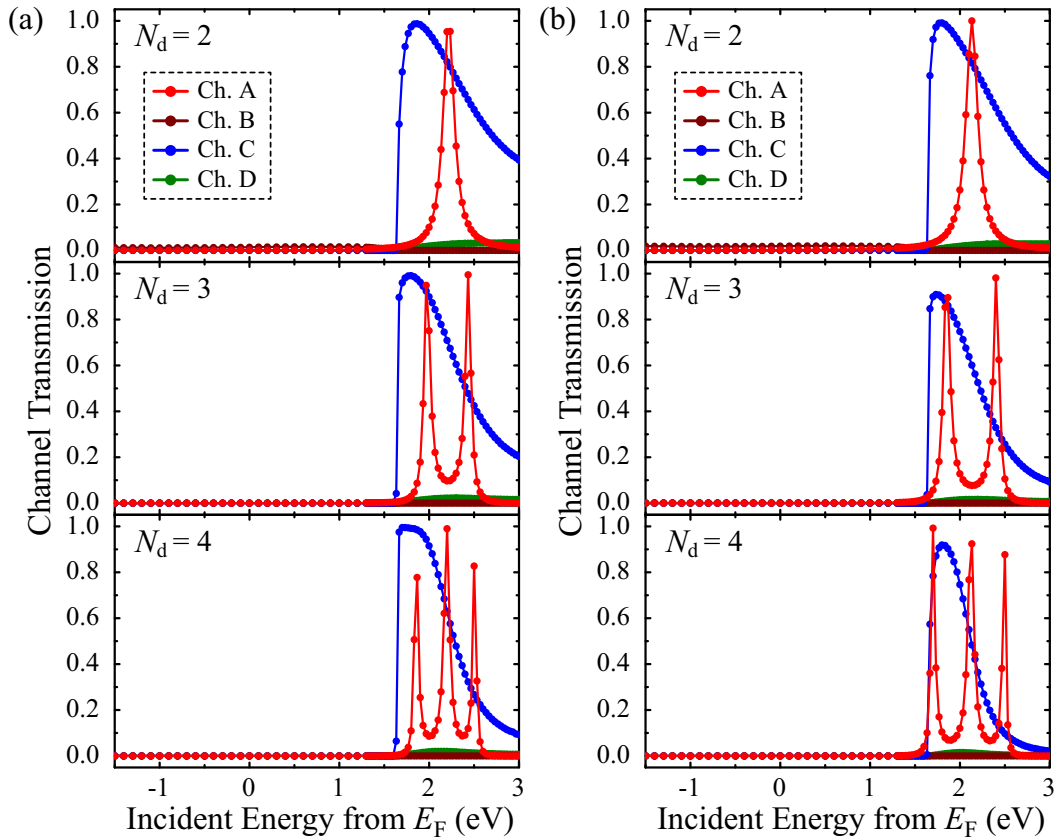


FIG. 5. Channel transmission profiles as functions of the incident electron energy measured from the Fermi energy  $E_F$  for the (a) CFG and (b) IFG models.

is sampled using a  $20(10) \times 1 \times 1$   $k$ -point grid for the CFG (IFG) model. The exchange-correlation effects are treated by the local density approximation [30], and the interaction between the electrons and the atomic cores is described by the norm-conserving pseudopotentials of Troullier and Martins [29,40].

We next examine the electron-transport properties of each fluorinated graphene connected to semi-infinite graphene electrodes. The scattering wave functions and the transmission coefficients are computed by using the overbridging boundary-matching method [18,19] with the proposed procedures. As shown in Fig. 4, the length of the supercell in the  $x$  direction for the IFG model is extended to twice that for the CFG model, where the generalized Bloch states and the self-energy matrices in the large electrodes for the extended model are constructed from those in the small model in accordance with the proposed method in Sec. II. We first calculate the electronic structure of the models by using periodic boundary conditions and then compute the scattering wave functions. For the CFG (IFG) model, the number of grid points in the scattering region is  $20(40) \times 60 \times 176$  and  $N_F$  is 4. On the other hand, in the electrode region of the CFG (IFG) model which contains 4 (8) C atoms, the cell lengths are taken as  $4.26(8.52) \times 12.7 \times 2.46 \text{ \AA}^3$  and the number of grid points is  $20(40) \times 60 \times 16$ . The Brillouin zone is sampled with the  $20(10)$   $k$ -point mesh for the CFG (IFG) model to evaluate the Kohn-Sham effective potential under the periodic boundary

condition. The conductance per unit cell under zero temperature and zero bias is described by the Landauer-Büttiker formula. To obtain a deeper understanding of the transport properties, the eigenchannels are computed by diagonalizing the Hermitian matrix  $\mathbf{T}^\dagger \mathbf{T}$  [41], where  $\mathbf{T}$  is the transmission matrix.

Figure 5 plots the channel transmission of the CFG and IFG models with  $N_d = 2, 3$ , and 4 as a function of the energy of the incident electrons  $E_{in}$ . For the CFG (IFG) model we evaluate the transport properties of electrons with  $k_x = 0$  and  $0.5$  ( $k_x = 0$ ) in the unit of  $2\pi/L_x$ , where  $k_x$  and  $L_x$  are the Bloch wave number and the cell length in the  $x$  direction, respectively. The generalized Bloch states and the self-energy matrices with  $k_x = 0$  in the semi-infinite graphene electrodes for the IFG model are comprised of those with  $k_x = 0$  and  $0.5$  for the CFG model using the formalism proposed in Sec. II. We confirm that the relative errors between the channel transmission probabilities evaluated with the self-energy matrices generated by using Eq. (5) with that reproduced by using Eq. (18) are lower than  $10^{-10}$ . In the CFG model, channels A and B are the profiles for incident electrons with  $k_x = 0$ . The profiles of the other channels are obtained from the results for the incident electrons with  $k_x = 0.5$ .

In the profiles there are mainly two conduction channels (i.e., channels A and C) with high transmission peaks in the energy range between  $E_F + 1.6 \text{ eV}$  and  $E_F + 3.0 \text{ eV}$  while the transmission probabilities are almost zero in a wide energy

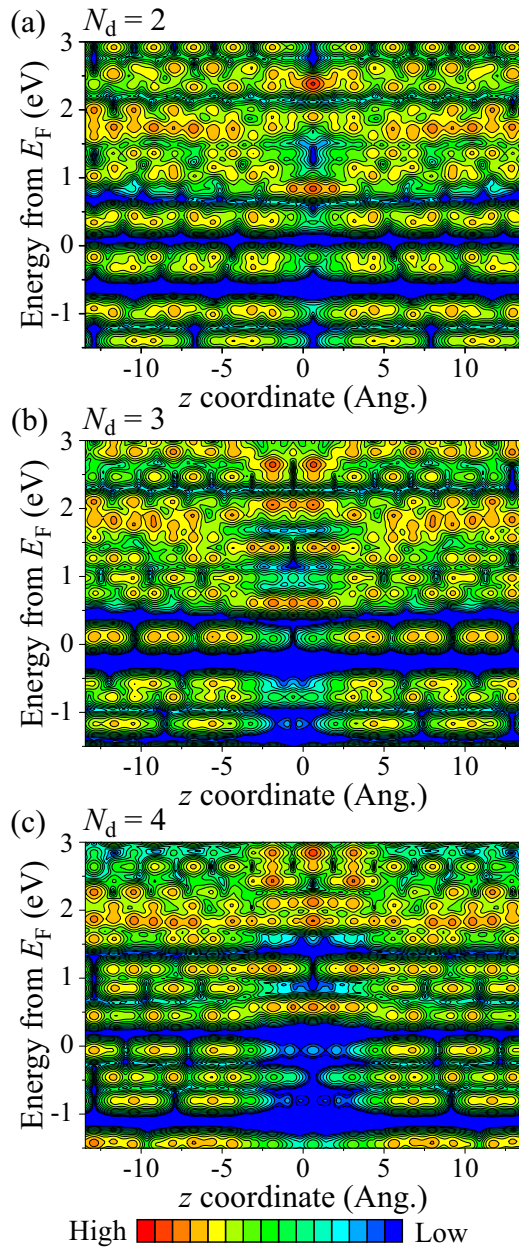


FIG. 6. Contour plots of LDOS for the IFG model with (a)  $N_d = 2$  and  $k_x = 0$ , (b)  $N_d = 3$  and  $k_x = 0$ , and (c)  $N_d = 4$  and  $k_x = 0$ . The energies are measured from the Fermi energy  $E_F$ . Each contour represents twice or half the density of the adjacent contours. The lowest contour is  $4.23 \times 10^{-8}$  electron/eV  $\text{\AA}^{-1}$ .

range near the Fermi energy  $E_F$ . To reveal the influence of the adatoms on the electron transport, we analyzed the local density of states (LDOS) of models as shown in Fig. 6 where the LDOS for the IFG model is drawn. The LDOS is plotted by integrating them along the  $xy$  plane,  $\rho(z, k_x, E) = \int |\Psi(\mathbf{r}, k_x, E)|^2 d\mathbf{r}_{\parallel}$ , where  $\mathbf{r} = (x, y, z)$ ,  $\mathbf{r}_{\parallel} = (x, y)$ ,  $\Psi$  is the wave function obtained by the electronic structure calculation, and  $E$  is the energy of the state. No transmission peaks exist in Fig. 5 despite the presence of the LDOS around the Fermi level (Fig. 6). In the vicinity of the Fermi level, high densities of states are observed around the fluorinated region, but decrease toward the pristine region. This result suggests

that the states localized at the fluorinated region are coupled to the evanescent wave in the pristine graphene. Therefore, these localized states do not contribute to the electron transport. On the other hand, at  $E_F + 1.6$  eV or more, the densities of the states around the fluorinated region extend to the graphene without attenuation, thus indicating that the states are successfully coupled with the propagating wave in the graphene. These states play important roles in the appearance of the transmission peaks. The same interpretation can be made for the CFG model.

Channel A has several peaks in the transmission profile, and the number of peaks increases with  $N_d$  while channel C has only one peak at approximately  $E_F + 1.8$  eV regardless of the  $N_d$  value. We will discuss the IFG model in the following, for simplicity. In order to explore the relationship between the number of peaks and  $N_d$ , the spatial distributions of the scattering wave functions with the incident energy at each transmission peak are revealed in Fig. 7.

It is found that channels A and C are classified according to the symmetry of the scattering wave function in the  $x$  direction. These characteristics should reflect the incident Bloch states in the electrode region and the electronic structure in the transition region. Figure 8 shows the energy band structure and the spatial distributions of the Bloch states constituting subbands in the graphene electrode. The states of bands A, C, and D contribute to the incident Bloch states exhibiting the transmission peaks in the energy range of  $E_F + 1.6$  eV to  $E_F + 3.0$  eV [Fig. 8(a)].

The spatial distributions of the wave function  $\Psi(\mathbf{r}, k_x, E)$  at the energy level of  $E_F + 1.6$  eV to  $E_F + 3.0$  eV are represented in Fig. 9 for the IFG model with  $N_d = 4$ . The Bloch state constituting band A [Fig. 8(b)] has the same symmetry in the  $x$  direction as the states depicted in Figs. 9(a)–9(c). On the contrary, the symmetry in the  $x$  direction of the Bloch state in band D [Fig. 8(f)] is the same as the symmetry of the state as shown in Fig. 9(d). Thus, the incident Bloch states smoothly connect to the states in the transition region. Furthermore, when the  $z$  component of the wave vector determined by the incident energy matches the wave number of the wave function allowed in the transition region, the transmission profile exhibits peaks. The number of the allowed wave number is proportional to  $N_d$ . Similar conclusions are obtained for the other models.

In the profiles of channel A, there are no significant differences in the channel transmission profiles between the CFG and IFG models while the peak positions for the IFG model are slightly shifted toward a lower energy compared to those for the CFG model. By contrast, with regard to channel C, the transmission probability reaches almost unity in the CFG model, while the peak value remains at approximately 0.9 in the IFG model with a large  $N_d$ . The atomic geometry and the electronic structure of the IFG model have mirror symmetry with respect to the center in the  $x$  direction of the cell [Fig. 4(c)] although the Bloch states in the graphene electrode have the translational symmetry in the  $x$  direction (Fig. 8). This discrepancy in the symmetry is considered to prevent unity of the transmission probability.

As mentioned earlier, the adsorption of fluorine atoms on the graphene surface effectively inhibits electron transport near the Fermi level. The number of fluorinated carbon dimers

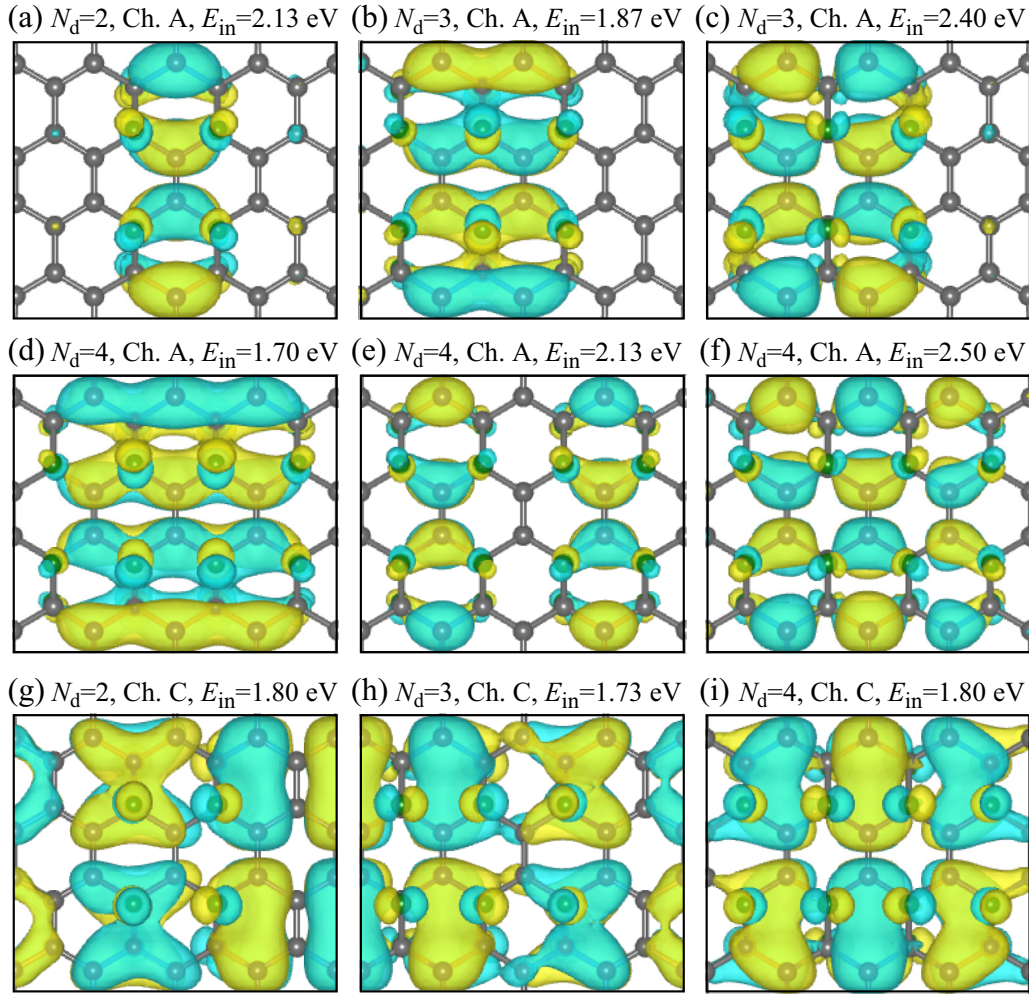


FIG. 7. Distribution of the scattering wave function for the IFG model. (a)–(f) and (g)–(i) Depict the scattering wave functions for the electrons with incident energy that peaks the transmission profile of channels A and C in Fig. 5(b), respectively.  $E_{in}$  refers to the incident energy measured from  $E_F$ . The key to the symbols is the same as that in Fig. 4. The value of the yellow (blue) isosurface is 0.03 (–0.03) a.u. for channel A and 0.005 (–0.005) a.u. for channel C.

aligned in the transport ( $z$ ) direction  $N_d$  is important for evaluating the electron-transport properties of the presented models. The symmetry of the atomic geometry in the  $x$  direction affects the peak value of the transmission profile. In addition, it is expected that the energy interval of the peaks can be tuned depending on the arrangement of the fluorinated carbon dimer in the  $z$  direction.

#### IV. CONCLUSION

We proposed herein an improved algorithm for preparing the self-energy matrices for the first-principles electron-transport property calculations. In the conventional procedure, the computational cost of the self-energy matrices increased proportionally to the cubic of the transversal length of the electrodes surface because the inverse matrix calculations were required. By contrast, in the proposed procedure, the self-energy matrices of the large electrode unit cell where the primitive unit cell was repeated in the directions parallel

to the electrode surface can be accurately reproduced from the calculations for the small primitive unit cell. We also demonstrated the accuracy of the reconstructed self-energy matrices employing the Si(001) bulk system and verified that our procedure can reduce the computational costs in constructing the self-energy matrices of a large electrode without deteriorating accuracy.

On the basis of the proposed procedure, we performed electron-transport calculations of the fluorinated graphene system and investigated the dependency of the transport properties on the density and arrangement of adatoms. In the transport calculation, fluorinated graphene was connected to semi-infinite graphene electrodes, where the self-energy matrices of the large graphene electrodes were efficiently constructed based on the generalized Bloch states of the small graphene electrodes. The calculations revealed that fluorination of graphene surface suppresses the transmission probability near the Fermi level. The results of the density of states calculations in the transition region showed that the

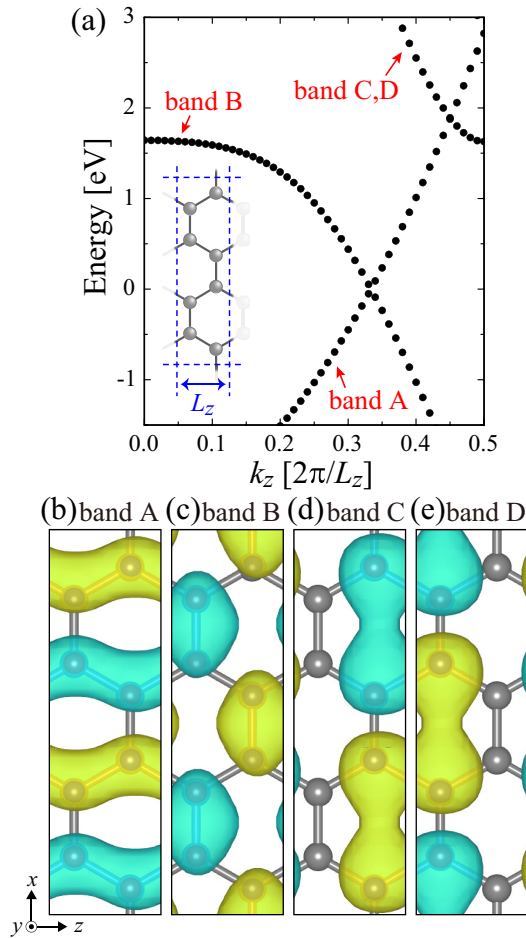


FIG. 8. Energy band structure in the infinite graphene and spatial distributions of the Bloch wave functions. In (a) the energy band structure is calculated using the unit cell represented by the inset figure, where blue dashed lines indicate the cell boundaries. Energy bands C and D are degenerated. In (b)–(e) the Bloch wave functions of band A at  $k_z = 0$ , band B at  $k_z = 0$ , band C at  $k_z = 0.5$ , and band D at  $k_z = 0.5$  are illustrated, respectively. The value of the yellow (blue) isosurface is 0.05 (−0.05) a.u. The key to the symbols is the same as that in Fig. 4.

transmission was significantly impaired because the incident Bloch states cannot be successfully coupled with the states of the transition region. On the other hand, two conduction channels had high transmission peaks in the region of high incident energy. The differences in the electron-transmission dependency on the density and arrangement of adatoms between these channels can be explained from the symmetry of the electronic structures of the transition regions calculated under periodic boundary conditions and the generalized Bloch states of the semi-infinite electrodes. The interpretation of the electron-transport properties of the fluorinated graphene utilizing symmetry is expected to be applied to other systems, such as those containing other adatoms or substitutional impurities and materials other than graphene as well.

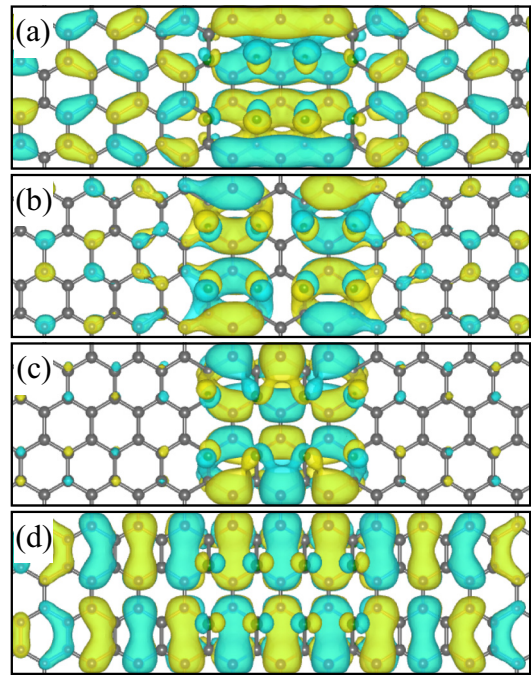


FIG. 9. Distributions of wave functions for the IFG model with  $N_d = 4$  at the energy of (a)  $E = E_F + 1.77$  eV, (b)  $E = E_F + 2.08$  eV, (c)  $E = E_F + 2.49$  eV, and (d)  $E = E_F + 2.29$  eV. The key to the symbols is the same as that in Fig. 4. The value of the yellow (blue) isosurface is 0.01 (−0.01) a.u.

## ACKNOWLEDGMENTS

Y.E. acknowledges the financial support from JSPS KAKENHI Grant No. JP18K04873. S.T. acknowledges the financial support from Deutsche Forschungsgemeinschaft through the Collaborative Research Center SFB 1238 (Project C01). T.O. acknowledges the financial support from MEXT as a social and scientific priority issue (creation of new functional devices and high performance materials to support next-generation industries) to be tackled by using post-K computer and JSPS KAKENHI Grant No. JP16H03865. The numerical calculations were carried out using the system B and the system C of the Institute for Solid State Physics at the University of Tokyo, the COMA of the Center for Computational Sciences at University of Tsukuba, and the K computer provided by the RIKEN Advanced Institute for Computational Science through the HPCI System Research project (Project ID: hp180226).

## APPENDIX A: IMPROVING ACCURACY OF THE TRANSMISSION COEFFICIENT

In the wave-function matching method, the transmission coefficients are obtained by decomposing a scattering wave function into the generalized Bloch wave functions of an electrode. The accuracy of the coefficients is known to deteriorate if a scattering wave function contains decaying generalized Bloch wave components, because the generalized Bloch wave functions are not orthogonal to each other. In this Appendix, aiming at improving the accuracy of the transmission coefficients, we propose an effective procedure to calculate them

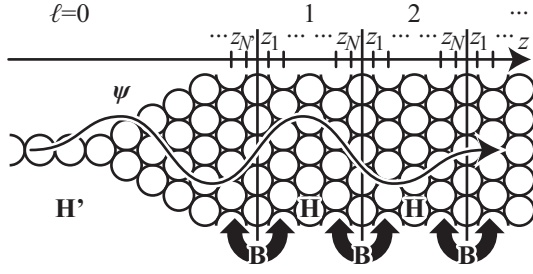


FIG. 10. Schematic representation of a system used for the transport calculations.  $\ell = 0$  indicates the transition region, and  $\ell > 0$  denotes the electrode unit cell at the right-hand side of the transition region.  $N'$  and  $\mathbf{H}'$  represent the number of the real-space grids along the  $z$  direction and the truncated Hamiltonian of the transition region, respectively.  $\mathbf{H}$  and  $\mathbf{B}$  are the same as those in Fig. 1.

from a scattering wave function deep inside an electrode, where the rightward decaying generalized Bloch wave components of it vanish and it is expressed as a linear combination only of the rightward propagating generalized Bloch wave functions of the electrode. The coefficients for the linear combination are just the transmission coefficients. Since the number of rightward propagating/decaying generalized Bloch states in an electrode is  $N_B$  [22] as defined in Sec. II, the number of transmission coefficients is also  $N_B$ , and then, we hereafter express the set of the transmission coefficients as a column vector  $\mathbf{t} = [t_1, t_2, \dots, t_{N_B}]^T$ .

### 1. Calculating a transmission coefficient inside an electrode

We show in the following that the transmission coefficients can be obtained from a scattering wave function at the interface between two electrode unit cells indicated by  $\ell = 1$  and  $2$  in Fig. 10, whereas they have been so far evaluated from a scattering wave function at the interface between the transition region ( $\ell = 0$  in Fig. 10) and the adjoining electrode unit cell ( $\ell = 1$  in Fig. 10). A scattering wave function in the first electrode unit cell ( $\ell = 1$ ) is known to satisfy the following Kohn-Sham equation:

$$(\varepsilon - \mathbf{H}) \begin{bmatrix} \psi_{1,1} \\ \vdots \\ \psi_{1,N} \end{bmatrix} = \begin{bmatrix} -\mathbf{B}^\dagger \psi_{0,N} \\ 0 \\ \vdots \\ 0 \\ -\mathbf{B} \psi_{2,1} \end{bmatrix}, \quad (\text{A1})$$

where  $\mathbf{H}$  denotes the truncated Hamiltonian matrix of an electrode unit cell, and  $\mathbf{B}$  represents the interaction between the adjoining electrode unit cells (see Fig. 10). Note that the interaction between the transition region and the next electrode unit cell is assumed to be identical to that between the adjoining electrode unit cells, and is represented by  $\mathbf{B}$ . The subvectors  $\psi_{\ell,1}$  and  $\psi_{\ell,N}$  represent the portions of the scattering wave function at  $z = z_1$  and  $z = z_N$  in the  $\ell$ th unit cell, respectively. By defining the Green's function matrix as  $\mathbf{G} = (\varepsilon - \mathbf{H})^{-1}$ , the Kohn-Sham equation above is rewritten

as

$$\begin{bmatrix} \psi_{1,1} \\ \vdots \\ \psi_{1,N} \end{bmatrix} = \begin{bmatrix} \mathbf{G}_{11} & \dots & \dots & \dots & \mathbf{G}_{1N} \\ \vdots & \ddots & & & \vdots \\ \vdots & & \ddots & & \vdots \\ \vdots & & & \ddots & \vdots \\ \mathbf{G}_{N1} & \dots & \dots & \dots & \mathbf{G}_{NN} \end{bmatrix} \begin{bmatrix} -\mathbf{B}^\dagger \psi_{0,N} \\ 0 \\ \vdots \\ 0 \\ -\mathbf{B} \psi_{2,1} \end{bmatrix}, \quad (\text{A2})$$

where  $\mathbf{G}_{11}$ ,  $\mathbf{G}_{1N}$ ,  $\mathbf{G}_{N1}$ , and  $\mathbf{G}_{NN}$  are the  $N_B$ -dimensional submatrices of  $\mathbf{G}$  found at the top-left, top-right, bottom-left, and bottom-right corners, respectively. The last block-row of the equation above reads

$$\psi_{1,N} = -\mathbf{G}_{N1} \mathbf{B}^\dagger \psi_{0,N} - \mathbf{G}_{NN} \mathbf{B} \psi_{2,1}. \quad (\text{A3})$$

We now expand the scattering wave functions  $\psi_{1,N}$  and  $\psi_{2,1}$  with the rightward propagating/decaying generalized Bloch wave functions of the electrode unit cell as follows:

$$\psi_{1,N} = \sum_{i=1}^{N_B} t_i \mathbf{q}_{i,1,N}, \quad (\text{A4})$$

$$\psi_{2,1} = \sum_{i=1}^{N_B} t_i \mathbf{q}_{i,2,1} = \sum_{i=1}^{N_B} t_i \lambda_i \mathbf{q}_{i,1,1}. \quad (\text{A5})$$

$\lambda_i$  denotes the phase factor of the  $i$ th generalized Bloch state. Substituting Eqs. (A4) and (A5) for Eq. (A3), we can derive the following linear equation with respect to  $\mathbf{t}$ :

$$[\mathbf{Q}_N + \mathbf{G}_{NN} \mathbf{B} \mathbf{Q}_1 \mathbf{\Lambda}] \mathbf{t} = -\mathbf{G}_{N1} \mathbf{B}^\dagger \psi_{0,N}, \quad (\text{A6})$$

where  $\mathbf{\Lambda}$  is the diagonal matrix composed of  $\lambda_i$  for  $i = 1, \dots, N_B$ . Solving the linear equation above, we can obtain the  $\mathbf{t}$  that is evaluated from a scattering wave function at the interface between the unit cells of  $\ell = 1$  and  $\ell = 2$ . In general, a scattering wave function is composed of propagating and decaying generalized Bloch waves. Among the decaying generalized Bloch wave components, quickly decaying ones are suppressed when the scattering wave reaches the interface between the unit cells of  $\ell = 1$  and  $\ell = 2$ , however, slowly decaying ones still survive. Therefore, the accuracy of  $\mathbf{t}$  obtained by solving Eq. (A6) is improved to some degree, but is not yet enough for a detailed investigation of the electron-transport properties; this issue will be discussed later in Appendix A3. To obtain a more accurate  $\mathbf{t}$ , we have to remove the slowly decaying generalized Bloch wave components from the scattering wave functions.

### 2. Green function of an elongated electrode unit cell

If we could combine multiple electrode unit cells in the  $z$  direction (see Fig. 10) and obtain the Green's function matrix of the large unit cell, we would be able to accurately calculate the transmission coefficient from the scattering wave function deep inside the electrode. However, it is obviously expensive and impractical to compute such a large Green's function matrix. In this subsection we discuss a more efficient procedure than the direct calculation of the Green's function matrix. According to Eq. (A6), one can see that to calculate  $\mathbf{t}$  we need only two  $N_B$ -dimensional square matrices at the bottom-left and bottom-right corners of the Green's function matrix of an

electrode unit cell. Therefore, we introduce a method to obtain the two  $N_B$ -dimensional square matrices without calculating the whole Green's function matrix of a large electrode unit cell elongated along the  $z$  direction. In the following we exemplify it with an electrode unit cell that is two times longer than that shown in Fig. 10. The Hamiltonian of the elongated electrode unit cell is simply expressed using  $\mathbf{H}$  and  $\mathbf{B}$  as

$$\varepsilon - \tilde{\mathbf{H}}^{(2)} = \begin{bmatrix} & & & 0 & \dots & 0 \\ & \varepsilon - \mathbf{H} & & 0 & \ddots & \vdots \\ & & & \mathbf{B} & 0 & 0 \\ 0 & 0 & \mathbf{B}^\dagger & & & \\ \vdots & \ddots & 0 & & \varepsilon - \mathbf{H} & \\ 0 & \dots & 0 & & & \end{bmatrix}. \quad (\text{A7})$$

Let us now think of deriving the Green's function matrix of the elongated electrode unit cell, i.e.,  $\tilde{\mathbf{G}}^{(2)} = (\varepsilon - \tilde{\mathbf{H}}^{(2)})^{-1}$ . According to Appendix B, the bottom-right quadrant of  $\tilde{\mathbf{G}}^{(2)}$  is expressed as

$$\tilde{\mathbf{G}}_{\text{BR}}^{(2)} = \left( \varepsilon - \mathbf{H} - \begin{bmatrix} \mathbf{B}^\dagger \mathbf{G}_{\text{NN}} \mathbf{B} & \mathbf{0} & \mathbf{0} \\ \mathbf{0} & \ddots & \vdots \\ \mathbf{0} & \dots & \mathbf{0} \end{bmatrix} \right)^{-1}. \quad (\text{A8})$$

The  $N_B$ -dimensional submatrix at the bottom-right corner of  $\tilde{\mathbf{G}}^{(2)}$  is found at the bottom-right corner of the inverse matrix on the right-hand side of the equation above. The former is referred to as  $\tilde{\mathbf{G}}_{\text{NN}}^{(2)}$ , and the latter as  $\tilde{\mathbf{G}}_{\text{BR,NN}}^{(2)}$ . According to Appendix C,  $\tilde{\mathbf{G}}_{\text{BR,NN}}^{(2)}$  can be analytically derived as

$$\begin{aligned} \tilde{\mathbf{G}}_{\text{NN}}^{(2)} &= \tilde{\mathbf{G}}_{\text{BR,NN}}^{(2)} \\ &= \mathbf{G}_{\text{NN}} + \mathbf{G}_{\text{N1}} \mathbf{B}^\dagger \mathbf{G}_{\text{NN}} \mathbf{B} \\ &\quad \times [\mathbf{I} - \mathbf{G}_{\text{11}} \mathbf{B}^\dagger \mathbf{G}_{\text{NN}} \mathbf{B}]^{-1} \mathbf{G}_{\text{1N}}, \end{aligned} \quad (\text{A9})$$

where  $\mathbf{I}$  denotes the  $N_B$ -dimensional identity matrix. In a similar way, using Eqs. (B1) and (B2), the bottom-left quadrant of  $\tilde{\mathbf{G}}^{(2)}$  is expressed as

$$\tilde{\mathbf{G}}_{\text{BL}}^{(2)} = -\tilde{\mathbf{G}}_{\text{BR}}^{(2)} \begin{bmatrix} \mathbf{B}^\dagger \mathbf{G}_{\text{N1}} & \dots & \mathbf{B}^\dagger \mathbf{G}_{\text{NN}} \\ \mathbf{0} & \dots & \mathbf{0} \\ \mathbf{0} & \dots & \mathbf{0} \end{bmatrix}. \quad (\text{A10})$$

Since the  $N_B$ -dimensional submatrix at the bottom-left corner of  $\tilde{\mathbf{G}}^{(2)}$ , which is referred to as  $\tilde{\mathbf{G}}_{\text{N1}}^{(2)}$ , is found at the bottom-left corner of the matrix on the right-hand side of the equation above, it is given as

$$\tilde{\mathbf{G}}_{\text{N1}}^{(2)} = \tilde{\mathbf{G}}_{\text{BL,N1}}^{(2)} = -\tilde{\mathbf{G}}_{\text{BR,N1}}^{(2)} \mathbf{B}^\dagger \mathbf{G}_{\text{N1}}, \quad (\text{A11})$$

where  $\tilde{\mathbf{G}}_{\text{BL,N1}}^{(2)}$  and  $\tilde{\mathbf{G}}_{\text{BR,N1}}^{(2)}$  represent the  $N_B$ -dimensional submatrices at the bottom-left corner of  $\tilde{\mathbf{G}}_{\text{BL}}^{(2)}$  and  $\tilde{\mathbf{G}}_{\text{BR}}^{(2)}$ , respectively. According to Appendix C,  $\tilde{\mathbf{G}}_{\text{BR,N1}}^{(2)}$  can be analytically derived as

$$\tilde{\mathbf{G}}_{\text{BR,N1}}^{(2)} = \mathbf{G}_{\text{N1}} [\mathbf{I} - \mathbf{B}^\dagger \mathbf{G}_{\text{NN}} \mathbf{B} \mathbf{G}_{\text{11}}]^{-1}. \quad (\text{A12})$$

Therefore, we finally obtain

$$\tilde{\mathbf{G}}_{\text{N1}}^{(2)} = -\mathbf{G}_{\text{N1}} [\mathbf{I} - \mathbf{B}^\dagger \mathbf{G}_{\text{NN}} \mathbf{B} \mathbf{G}_{\text{11}}]^{-1} \mathbf{B}^\dagger \mathbf{G}_{\text{N1}}. \quad (\text{A13})$$

Using  $\tilde{\mathbf{G}}_{\text{N1}}^{(2)}$  defined at Eq. (A13) and  $\tilde{\mathbf{G}}_{\text{NN}}^{(2)}$  defined at Eq. (A9), one can derive the equation describing the relation among the

scattering wave function subvectors  $\psi_{2,N}$ ,  $\psi_{0,N}$ , and  $\psi_{3,1}$  as

$$\psi_{2,N} = -\tilde{\mathbf{G}}_{\text{N1}}^{(2)} \mathbf{B}^\dagger \psi_{0,N} - \tilde{\mathbf{G}}_{\text{NN}}^{(2)} \mathbf{B} \psi_{3,1}. \quad (\text{A14})$$

In analogy with Eqs. (A4) and (A5),  $\psi_{2,N}$  and  $\psi_{3,1}$  are expressed as the linear combinations of the rightward propagating/decaying generalized Bloch waves:

$$\psi_{2,N} = \sum_{i=1}^{N_B} t_i \mathbf{q}_{i,2,N} = \sum_{i=1}^{N_B} t_i \lambda_i \mathbf{q}_{i,1,N}, \quad (\text{A15})$$

$$\psi_{3,1} = \sum_{i=1}^{N_B} t_i \mathbf{q}_{i,3,1} = \sum_{i=1}^{N_B} t_i \lambda_i^2 \mathbf{q}_{i,1,1}. \quad (\text{A16})$$

Substituting Eqs. (A15) and (A16) for Eq. (A14), one finally obtains the linear equation for  $t$  of the scattering wave function at the interface between the unit cells of  $\ell = 2$  and  $\ell = 3$ :

$$[\mathbf{Q}_N \Lambda + \tilde{\mathbf{G}}_{\text{NN}}^{(2)} \mathbf{B} \mathbf{Q}_1 \Lambda^2] t = -\tilde{\mathbf{G}}_{\text{N1}}^{(2)} \mathbf{B}^\dagger \psi_{0,N}. \quad (\text{A17})$$

Extending the aforementioned discussion to be  $n > 2$ , we can derive the general form of Eq. (A6) as

$$[\mathbf{Q}_N \Lambda^{n-1} + \tilde{\mathbf{G}}_{\text{NN}}^{(n)} \mathbf{B} \mathbf{Q}_1 \Lambda^n] t = -\tilde{\mathbf{G}}_{\text{N1}}^{(n)} \mathbf{B}^\dagger \psi_{0,N}, \quad (\text{A18})$$

in which  $t$  is evaluated from the scattering wave function at the interface between the unit cells of  $\ell = n$  and  $\ell = n + 1$ , where any rightward decaying generalized Bloch wave components of the scattering wave function must be negligibly small.  $\tilde{\mathbf{G}}_{\text{N1}}^{(n)}$  and  $\tilde{\mathbf{G}}_{\text{NN}}^{(n)}$  can be straightforwardly obtained by repeating the procedure mentioned in this subsection. It should be noticed that the aforementioned discussion about the transmission coefficients is also applicable for accurately calculating the reflection coefficients.

### 3. Accuracy test

To validate the procedure discussed in the previous sections, we evaluate accuracy of the transmission coefficients of a simple Al atomic chain containing a single Si atom as an impurity. The model used for the accuracy evaluation is depicted in Fig. 11(a). The dimensions of the unit cell in the direction perpendicular to the chain axis are set to  $L_x = 16 a_B$  and  $L_y = 16 a_B$  for both electrode and transition regions. The length of the unit cell is  $L_z = 5.6 a_B$  for the electrode region, and  $L_z = N_S \times 5.6 a_B$  for the transition region.  $N_S$  denotes the number of atoms included in the transition region that varied from three and five in this evaluation. The position impurity Si atom is fixed at the second from the left. In calculating the transmission coefficients, the Green's function submatrices  $\tilde{\mathbf{G}}_{\text{NN}}^{(n)}$  and  $\tilde{\mathbf{G}}_{\text{N1}}^{(n)}$  in Eq. (A18) are evaluated for  $n = N_R$ , and therefore, the transmission coefficients are obtained from the scattering wave functions at the interface between the  $N_R$ th and  $(N_R + 1)$ th electrode unit cells. Note that in the case of  $N_R = 0$  the transmission coefficients are evaluated from the scattering wave function at the interface between the transition region and the neighboring electrode unit cell. The effective potential of the electrode unit cell of the chain system is calculated by the RSPACE code with  $1 \times 1 \times 60 k$  points. For the transition region, the effective potential is calculated with  $1 \times 1 \times 20$ ,  $1 \times 1 \times 15$ , and  $1 \times 1 \times 12 k$  points for  $N_R = 3, 4$ , and  $5$ , respectively. The calculations are carried out with norm-conserving pseudopotentials [28,29] and with

(a) calculation model

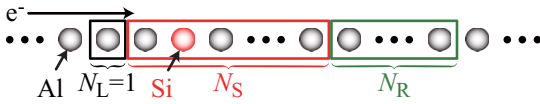
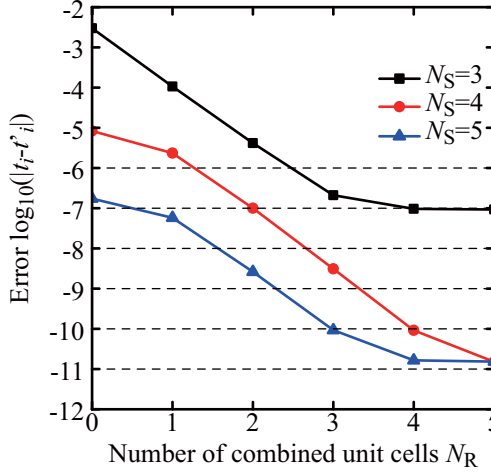
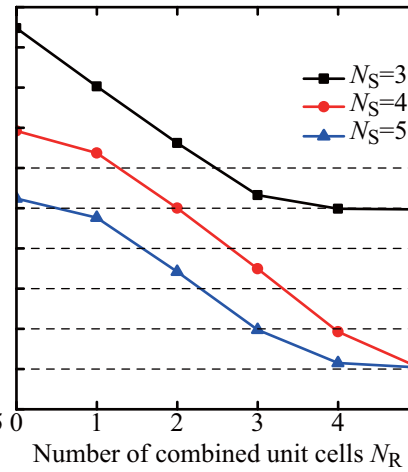
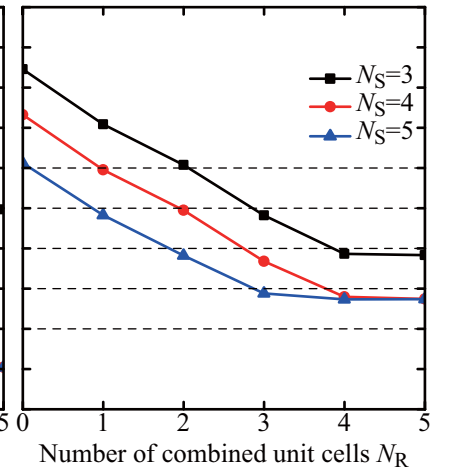
(b) 1st transmission channel ( $i=1$ )(c) 2nd transmission channel ( $i=2$ )(d) 3rd transmission channel ( $i=3$ )

FIG. 11. Computational error in the transmission coefficients. (a) The schematic representation of an atomic chain model used for the accuracy test. The chain is composed of Al atoms and a single Si atom as an impurity. In the calculation of the transmission coefficients,  $N_R$  electrode unit cells are combined, and the Green's function submatrices are calculated. (b)–(d) The errors in the transmission coefficients for the first, second, and third transmission channels, respectively. The computational error is evaluated with respect to the transmission coefficient obtained for  $N_S = 8$  and  $N_R = 0$ . Note that in this context the transmission coefficients are calculated from the scattering wave function at the interface between the electrode unit cells of  $\ell = N_R$  and  $\ell = N_R + 1$ , e.g., the scattering wave function at the interface between the transition region and the first electrode unit cell is used for calculating the transmission coefficients for  $N_R = 0$ . The dashed horizontal lines are guide for the eyes.

the local-density approximation [30] within the framework of the density functional theory.

Figures 11(b)–11(d) show the error in the transmission coefficient as a function of the number of electrode unit cells combined for the first, second, and third channels, respectively. The computational error is evaluated by  $|t_i - t'_i|$ , where  $t_i$  denotes the calculated transmission coefficient of the  $i$ th channel,  $t'_i$  is the reference one.  $t'_i$  is calculated for  $N_S = 8$  and without using Eq. (A18), i.e.,  $N_R = 0$ . We have confirmed that in comparison to the case of  $N_S = 8$  and  $N_R = 5$ ,  $t'_i$  is accurate down to the 11th, 11th, and 9th decimal places for the first, second, and third channels, respectively. From Figs. 11(b)–11(d), it is clearly seen that in the case of  $N_S = 3$  the transition region is too short to evaluate the error in the transmission coefficient. This would be attributed to the effective potential at the right end of the transition region, which does not yet converge to that of the electrode unit cell. We need to include more electrode unit cells at the end of the transition region. In cases of  $N_S = 3$  and 4, the error in the transmission coefficients monotonically decreases as a function of  $N_R$ , and reaches the accuracy limit mentioned above at  $N_R = 5$ . One can see the fact that the accuracy is almost the same when  $N_S + N_R$  is identical, e.g.,  $(N_S, N_R) = (3, 3), (4, 2), (5, 1)$  in Fig. 11(d). This result implies that we can reduce the length of the transition region to as short as possible if we use the procedure mentioned in the previous sections for calculating transmission/reflection coefficients. Consequently, we can conclude that the procedure proposed in this section contributes not only an accurate calculation of the

transmission/reflection coefficients but also a less expensive computation of the scattering wave functions.

## APPENDIX B: INVERSE OF A $2 \times 2$ BLOCK MATRIX

It is already known that the inverse of a  $2 \times 2$  block matrix is expressed as [42]

$$\begin{bmatrix} \mathbf{A}_{11} & \mathbf{A}_{12} \\ \mathbf{A}_{21} & \mathbf{A}_{22} \end{bmatrix}^{-1} = \begin{bmatrix} \mathbf{C}_1^{-1} & -\mathbf{A}_{11}^{-1}\mathbf{A}_{12}\mathbf{C}_2^{-1} \\ -\mathbf{C}_2^{-1}\mathbf{A}_{21}\mathbf{A}_{11}^{-1} & \mathbf{C}_2^{-1} \end{bmatrix}, \quad (\text{B1})$$

where

$$\begin{aligned} \mathbf{C}_1 &= \mathbf{A}_{11} - \mathbf{A}_{12}\mathbf{A}_{22}^{-1}\mathbf{A}_{21}, \\ \mathbf{C}_2 &= \mathbf{A}_{22} - \mathbf{A}_{21}\mathbf{A}_{11}^{-1}\mathbf{A}_{12}. \end{aligned} \quad (\text{B2})$$

Note that  $\mathbf{A}_{11}$  and  $\mathbf{A}_{22}$  must both be invertible.

## APPENDIX C: DERIVATION OF EQS. (A9) AND (A13)

Here we show how to derive the analytic form of  $\tilde{\mathbf{G}}_{NN}^{(2)}$  in Eq. (A9) and  $\tilde{\mathbf{G}}_{N1}^{(2)}$  in Eq. (A13). It is convenient to start with a more general derivation of the submatrices at the four corners of an inverse matrix. First, let us think of the inverse of the following matrix:

$$\mathbf{A} = \mathbf{A}_0 - \begin{bmatrix} \Delta_L & \mathbf{0} & \mathbf{0} \\ \mathbf{0} & \mathbf{0} & \mathbf{0} \\ \mathbf{0} & \mathbf{0} & \Delta_R \end{bmatrix}. \quad (\text{C1})$$

The second term on the right-hand side looks like a perturbation to  $\mathbf{A}_0$  and has nonzero values only at the top-left and bottom-right corners. We define a square matrix  $\Delta_L$  ( $\Delta_R$ ) so that the nonzero entries at the top-left corner (bottom-right corner) are included in  $\Delta_L$  ( $\Delta_R$ ). The dimensions of  $\Delta_L$  and  $\Delta_R$  are represented by  $N_L$  and  $N_R$ , respectively. By defining  $\mathbf{X} = \mathbf{A}^{-1}$ ,  $\mathbf{A}\mathbf{X} = \mathbf{I}$  is rewritten as

$$\mathbf{A}_0\mathbf{X} = \mathbf{I} + \begin{bmatrix} \Delta_L & \mathbf{0} & \mathbf{0} \\ \mathbf{0} & \mathbf{0} & \mathbf{0} \\ \mathbf{0} & \mathbf{0} & \Delta_R \end{bmatrix} \mathbf{X}. \quad (\text{C2})$$

Multiplying both sides of the equation by  $\mathbf{Y} = \mathbf{A}_0^{-1}$  from the left, we obtain the following:

$$\mathbf{X} = \mathbf{Y} + \mathbf{Y} \begin{bmatrix} \Delta_L & \mathbf{0} & \mathbf{0} \\ \mathbf{0} & \mathbf{0} & \mathbf{0} \\ \mathbf{0} & \mathbf{0} & \Delta_R \end{bmatrix} \mathbf{X}. \quad (\text{C3})$$

From the matrix in each side, we extract the  $N_L \times N_L$ ,  $N_L \times N_R$ ,  $N_R \times N_L$ , and  $N_R \times N_R$  submatrices at the top-left, top-right, bottom-left, and bottom-right corners, respectively. Using these submatrices, we can construct the following  $(N_L + N_R)$ -dimensional matrix equation with respect to the submatrices of  $\mathbf{X}$ :

$$\mathbf{C} \begin{bmatrix} \mathbf{X}_{11} & \mathbf{X}_{1N} \\ \mathbf{X}_{N1} & \mathbf{X}_{NN} \end{bmatrix} = \begin{bmatrix} \mathbf{Y}_{11} & \mathbf{Y}_{1N} \\ \mathbf{Y}_{N1} & \mathbf{Y}_{NN} \end{bmatrix}, \quad (\text{C4})$$

where

$$\mathbf{C} = \begin{bmatrix} \mathbf{I} - \mathbf{Y}_{11}\Delta_L & -\mathbf{Y}_{1N}\Delta_R \\ -\mathbf{Y}_{N1}\Delta_L & \mathbf{I} - \mathbf{Y}_{NN}\Delta_R \end{bmatrix}. \quad (\text{C5})$$

Finally, the four submatrices of  $\mathbf{X}$  are given as

$$\begin{bmatrix} \mathbf{X}_{11} & \mathbf{X}_{1N} \\ \mathbf{X}_{N1} & \mathbf{X}_{NN} \end{bmatrix} = \mathbf{C}^{-1} \begin{bmatrix} \mathbf{Y}_{11} & \mathbf{Y}_{1N} \\ \mathbf{Y}_{N1} & \mathbf{Y}_{NN} \end{bmatrix}. \quad (\text{C6})$$

It is clearly seen that the submatrices of  $\mathbf{X}$  can be derived only from the four submatrices at the corners of  $\mathbf{Y}$ , i.e., we do not need to know all the entries of matrix  $\mathbf{Y}$ . The inverse matrix on the right-hand side of the equation above is in the form of a  $2 \times 2$  block matrix, and therefore, the discussion in Appendix B is applicable to the analytical calculation of the inverse.

Now let us apply the general discussion above to derive Eqs. (A9) and (A13). Substituting  $\mathbf{B}\mathbf{G}_{NN}\mathbf{B}$  for  $\Delta_L$ ,  $\mathbf{0}$  for  $\Delta_R$ ,  $\mathbf{G}_{ij}$  for  $\mathbf{Y}_{ij}$  (for  $i, j = 1, N$ ), and  $\tilde{\mathbf{G}}_{BR,ij}^{(2)}$  for  $\mathbf{X}_{ij}$  (for  $i, j = 1, N$ ), the inverse matrix on the right-hand side of Eq. (C6) is given as

$$\begin{bmatrix} \mathbf{I} - \mathbf{G}_{11}\mathbf{B}\mathbf{G}_{NN}\mathbf{B} & \mathbf{0} \\ -\mathbf{G}_{N1}\mathbf{B}\mathbf{G}_{NN}\mathbf{B} & \mathbf{I} \end{bmatrix}^{-1}. \quad (\text{C7})$$

Using the formula in Appendix B, one can easily calculate the inverse of this  $2 \times 2$  block matrix, and obtain the bottom-right and bottom-left quadrants of  $\tilde{\mathbf{G}}_{BR}^{(2)}$ , respectively. Consequently, one can determine  $\tilde{\mathbf{G}}_{NN}^{(2)}$  in Eq. (A9) and  $\tilde{\mathbf{G}}_{N1}^{(2)}$  in Eq. (A13).

- 
- [1] A. K. Geim, *Science* **324**, 1530 (2009).
- [2] F. Schedin, A. K. Geim, S. V. Morozov, E. W. Hill, P. Blake, M. I. Katsnelson, and K. S. Novoselov, *Nat. Mater.* **6**, 652 (2007).
- [3] O. Leenaerts, B. Partoens, and F. M. Peeters, *Phys. Rev. B* **77**, 125416 (2008).
- [4] K. T. Chan, J. B. Neaton, and M. L. Cohen, *Phys. Rev. B* **77**, 235430 (2008).
- [5] N. T. T. Tran, D. K. Nguyen, O. E. Glukhova, and M.-F. Lin, *Sci. Rep.* **7**, 17858 (2017).
- [6] O. V. Yazyev and S. G. Louie, *Nat. Mater.* **9**, 806 (2010).
- [7] D. L. Duong, G. H. Han, S. M. Lee, F. Gunes, E. S. Kim, S. T. Kim, H. Kim, Q. H. Ta, K. P. So, S. J. Yoon, S. J. Chae, Y. W. Jo, M. H. Park, S. H. Chae, S. C. Lim, J. Y. Choi, and Y. H. Lee, *Nature (London)* **490**, 235 (2012).
- [8] A. Lherbier, S. M.-M. Dubois, X. Declerck, Y.-M. Niquet, S. Roche, and J.-C. Charlier, *Phys. Rev. B* **86**, 075402 (2012).
- [9] S. Tsukamoto, T. Ono, and S. Blügel, *Phys. Rev. B* **97**, 115450 (2018).
- [10] A. Lherbier, X. Blase, Y.-M. Niquet, F. Triozan, and S. Roche, *Phys. Rev. Lett.* **101**, 036808 (2008).
- [11] T. Ono, T. Ota, and Y. Egami, *Phys. Rev. B* **84**, 224424 (2011).
- [12] R. Balog, B. Jørgensen, L. Nilsson, M. Andersen, E. Rienks, M. Bianchi, M. Fanetti, E. Lægsgaard, A. Baraldi, S. Lizzit, Z. Slijivancanin, F. Besenbacher, B. Hammer, T. G. Pedersen, H. Philip, and L. Hornekær, *Nat. Mater.* **9**, 315 (2010).
- [13] S. Latil, S. Roche, D. Mayou, and J.-C. Charlier, *Phys. Rev. Lett.* **92**, 256805 (2004).
- [14] T. B. Martins, R. H. Miwa, A. J. R. da Silva, and A. Fazzio, *Phys. Rev. Lett.* **98**, 196803 (2007).
- [15] H. H. B. Sørensen, P. C. Hansen, D. E. Petersen, S. Skelboe, and K. Stokbro, *Phys. Rev. B* **77**, 155301 (2008).
- [16] S. E. Laux, *Phys. Rev. B* **86**, 075103 (2012).
- [17] S. Brück, M. Calderara, M. H. Bani-Hashemian, J. VandeVondele, and M. Luisier, *J. Chem. Phys.* **147**, 074116 (2017).
- [18] K. Hirose, T. Ono, Y. Fujimoto, and S. Tsukamoto, *First-Principles Calculations in Real-Space Formalism* (Imperial College Press, London, 2005).
- [19] Y. Fujimoto and K. Hirose, *Phys. Rev. B* **67**, 195315 (2003).
- [20] J. R. Chelikowsky, N. Troullier, K. Wu, and Y. Saad, *Phys. Rev. B* **50**, 11355 (1994); J. R. Chelikowsky, N. Troullier, and Y. Saad, *Phys. Rev. Lett.* **72**, 1240 (1994).
- [21] W. Kohn, *Rev. Mod. Phys.* **71**, 1253 (1999); P. Hohenberg and W. Kohn, *Phys. Rev.* **136**, B864 (1964); W. Kohn and L. J. Sham, *ibid.* **140**, A1133 (1965).
- [22] S. Tsukamoto, K. Hirose, and S. Blügel, *Phys. Rev. E* **90**, 013306 (2014).
- [23] This is true only if  $\mathbf{B}$  is full rank. Even in the case of  $\mathbf{B}$  being rank deficient, this is true if a unitary transformation is applied to Eq. (1) so that the matrix corresponding to  $\mathbf{B}$  is full rank. For more details, see Ref. [22].
- [24] T. Ono, Y. Egami, and K. Hirose, *Phys. Rev. B* **86**, 195406 (2012).

- [25] W. H. Press, S. A. Teukolsky, W. T. Vetterling, and B. P. Flannery, *Numerical Recipes: The Art of Scientific Computing*, 3rd ed. (Cambridge University Press, New York, 2007); A. K. Cline and I. S. Dhillon, in *Handbook of Linear Algebra*, Discrete Mathematics and Its Applications, edited by L. Hogben (Chapman and Hall/CRC, Boca Raton, FL, 2006), Chap. 45, pp. 45.1–45.13; G. Golub and C. Reinsch, *Numer. Math.* **14**, 403 (1970).
- [26]  $a_B$  represents the unit of length in the atomic units, and  $1a_B = 0.529 \text{ \AA}$ .
- [27] T. Ono and K. Hirose, *Phys. Rev. B* **72**, 085115 (2005).
- [28] K. Kobayashi, *Comput. Mater. Sci.* **14**, 72 (1999).
- [29] N. Troullier and J. L. Martins, *Phys. Rev. B* **43**, 1993 (1991); L. Kleinman and D. M. Bylander, *Phys. Rev. Lett.* **48**, 1425 (1982).
- [30] S. H. Vosko, L. Wilk, and M. Nusair, *Can. J. Phys.* **58**, 1200 (1980).
- [31] K. S. Novoselov, A. K. Geim, S. V. Morozov, D. Jiang, Y. Zhang, S. V. Dubonos, I. V. Grigorieva, and A. A. Firsov, *Science* **306**, 666 (2004).
- [32] K. S. Novoselov, V. I. Fal'ko, L. Colombo, P. R. Gellert, M. G. Schwab, and K. Kim, *Nature (London)* **490**, 192 (2012).
- [33] A. K. Geim and K. S. Novoselov, *Nat. Mater.* **6**, 183 (2007).
- [34] M. H. F. Sluiter and Y. Kawazoe, *Phys. Rev. B* **68**, 085410 (2003).
- [35] J. O. Sofo, A. S. Chaudhari, and G. D. Barber, *Phys. Rev. B* **75**, 153401 (2007).
- [36] V. V. Ivanovskaya, A. Zobelli, D. Teillet-Billy, N. Rougeau, V. Sidis, and P. R. Briddon, *Eur. Phys. J. B* **76**, 481 (2010).
- [37] R. R. Nair, W. Ren, R. Jalil, I. Riaz, V. G. Kravets, L. Britnell, P. Blake, F. Schedin, A. S. Mayorov, S. Yuan, M. I. Katsnelson, H.-M. Cheng, W. Strupinski, L. G. Bulusheva, A. V. Okotrub, I. V. Grigorieva, A. N. Grigorenko, K. S. Novoselov, and A. K. Geim, *Small* **6**, 2877 (2010).
- [38] R. Zbořil, F. Karlický, A. B. Bourlinos, T. A. Steriotis, A. K. Stubos, V. Georgakilas, K. Šafářová, D. Jančík, C. Trapalis, and M. Otyepka, *Small* **6**, 2885 (2010).
- [39] W. Feng, P. Long, Y. Feng, and Y. Li, *Adv. Sci.* **3**, 1500413 (2016).
- [40] We used the norm-conserving pseudopotentials NCPS97 constructed by K. Kobayashi. See Ref. [28].
- [41] N. Kobayashi, M. Brandbyge, and M. Tsukada, *Phys. Rev. B* **62**, 8430 (2000); *Surf. Sci.* **433-435**, 854 (1999).
- [42] K. B. Petersen and M. S. Pedersen (2012), <http://www2.imm.dtu.dk/pubdb/p.php?3274>